Modeling & Performance Comparison of Screen-Printed, Impedance Spectroscopy Probes for Harsh Environments

Marios Sophocleous, Member, *IEEE*, Eduardo Garcia-Breijo, John K. Atkinson, and Julius Georgiou, Sr., *Member, IEEE*

***Abstract*—This paper compares the simulated performance of three different screen-printed probe geometries for Electrochemical Impedance Spectroscopy probes for use in harsh environments. The best performing probe, which is equipped with guarding electrodes that are proven to help with the electric field uniformity, shows a linear response with the medium's resistivity using a 1 kHz sinusoidal input current with a sensitivity of 0.163 mV/Ωm in the range of 2.5 Ωm to 50 Ωm in a medium with relative permittivity of 20. Additionally, the phase shift shows a linear relationship to the medium's relative permittivity and a sensitivity of 0.1 degrees/ε_r in the range of 5-81 using a 1 MHz sinusoidal input current. The equivalent circuit models of the probes were constructed and the values of the components have been reported. The best performing probe was fabricated and experimentally tested to back up the theoretical simulations and proposed models. The experimental and simulated values are within a ±6% error margin.**

***Index Terms*— Sensors, Thick-Film, Electrochemical Impedance Spectroscopy, Electric Field, Sensor Model, Electromagnetic Simulations.**

I. Introduction

THE CURRENT technological trend of connecting as many devices as possible to the Internet of Things (IoT), has created the need for real-time sensors in numerous applications [1], [2]. Integration of real-time sensors with IoT is, in some applications, the missing link in moving from open-loop to closed-loop control systems, which feature superior performances and are compatible with more sophisticated algorithms and machine learning techniques [3]. This allows the automation of a variety of tasks, currently requiring human presence and the even more expensive human labor. Although a plethora of sensors and sensing systems are available on the market, the environment in which those sensors can operate is, most of the times, limited to laboratory conditions. In even more challenging applications, the sensors are needed to operate not only out of the laboratory but also in extremely harsh environments [4]–[6].

Electrochemical Impedance Spectroscopy (EIS) is one of the most powerful techniques used for over a century for applications such as corrosion analysis, adsorption properties of molecules and quality monitoring of batteries and fuel cells [7]. In the vast majority of cases, this technique is used in the laboratory or other controlled environments because the probes/electrodes used lack the ability of operating in tough environments.

Usually, EIS probes are made of noble metals (e.g. platinum) or alloys (e.g. stainless steel) that do not oxidize with time so that their properties remain the same and any recorded changes are due to changes of the Material Under Test (MUT). The use of noble metals on one hand provides superior performance in terms of the probe's lifetime, but on the other hand, elevates the probes' cost. In order to overcome this, less expensive metals are used, to deliver the structural integrity of the probe, which are then electroplated/coated by noble metals such as gold, platinum or platinum black. In applications where high-density sensor networks are required, such as monitoring soil quality in the field or the structural integrity of concrete, the cost of the probe must be low enough to allow their implementation without a major capital investment [3]. Several technologies have been explored to provide robust sensors that can operate in such environments but they usually come at an elevated manufacturing cost. Thick-Film Technology (TFT) features a unique combination of low-cost sensors with exceptional robustness and reliability. Both physical (temperature, resistivity, water content) and chemical (pH) Thick-Film sensors have been demonstrated to operate in harsh environments such as soil and concrete [8]–[11]. TFT can be the answer to this problem because low-cost, screen-printed EIS probes using noble metals such as gold can be easily manufactured.

Other than the materials used, the probe's geometry plays an important role in their performance [12]. In applications like soil and concrete, the most common approach used is the

This work was supported by the University of Cyprus internal funds (Advanced Researchers Article 102).

Marios Sophocleous and Julius Georgiou are with the Department of Electrical & Computer Engineering, EMPHASIS Research Centre of the University of Cyprus, Nicosia, 2109, Cyprus (e-mail: sophocleous.marios@ucy.ac.cy, julio@ucy.ac.cy).

Eduardo Garcia-Breijo is with the Group of Electronic Development and Printed Sensors (GEDPS), Centro de Reconocimiento Molecular y Desarrollo Tecnológico, Unidad Mixta UPV-UV, Universitat Politècnica de Valéncia, Valencia 46022, Spain (e-mail: egarciab@eln.upv.es).

John K. Atkinson is with the Faculty of Engineering & Physical Sciences, University of Southampton, Southampton, SO17 1BJ, UK (e-mail: jka@soton.ac.uk).

four probe method using simple cylindrical rods in several configurations, such as the Wenner, Wenner-Schlumberger, Dipole-Dipole, Pole-Dipole and Pole-Pole, with the Weiner configuration being the most popular [13]–[19]. Although this geometry can cover a large volume of the MUT, the sensitivity is very low unless high power electronics are used. Due to the fact that the electric field propagates from a point source within the horizontal plane, the electric field strength at the sensing electrodes decreases dramatically [20]. Different geometries have been implemented, such as the three rods surrounding a central rod, which has been proven to have superior performance compared to the classical geometries, yet this geometry is only used for soil moisture content detection and not for soil conductivity/resistivity [21]. However, in situations where multiple types of sensors are required in soil or concrete, it is almost impossible to integrate other sensors on these rods without significantly affecting their performance. TFT-manufactured, planar probes can be used with other sensors integrated on the same substrate but they have significant drawbacks such as non-homogeneous electric fields, fringing of the electric field at different frequencies, different conductivities and different dielectric constants [10]. Therefore, a different approach is required to meet all the specifications required for a multisensor array in slurry and/or water-like mediums, such as soil and concrete.

In this paper, three different, screen-printed EIS probes have been constructed and simulated in mediums of various conductivities/resistivities and dielectric constants, showing how the drawbacks of planar probes can be overcome using 3D structures of screen-printed substrates as EIS probes. The results were used to construct equivalent circuits using common EIS models, whilst the electrical parameters of the models' components have been extracted and presented.

II. Theoretical Background

There are multiple methods in which EIS can be applied with the two most common being the bipolar and quadripolar electrode arrangements. The bipolar electrode arrangement is commonly used in applications where the electrodes can be calibrated or cleaned before the tests. In the cases that the same probe is to be used for longer lifetimes, the quadripolar electrode arrangement is mostly used [13].

In the quadripolar electrode arrangement, four electrodes are used as shown in Fig. 1.

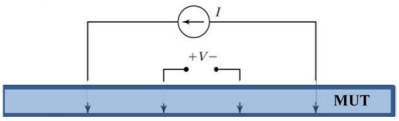

Fig. 1: Quadripolar electrode arrangement.

Assuming that the potential generated at the two electrodes connected to the voltmeter is proportional to the voltage applied at the interface between the MUT and the current electrodes, then the voltage measured at the voltage electrodes can be used to calculate the impedance of the MUT. If a sinusoidal source is used, then the impedance of the MUT can be calculated by [22]:

$$Z(\omega) = \frac{E_0}{I_0} e^{j\varphi(\omega)} = Z_0 e^{j\varphi(\omega)} = Z_0 \cos\varphi(\omega) + jZ_0 \sin\varphi(\omega) \qquad (1)$$

where $Z(\omega)$ is the complex impedance of the MUT at any frequency, ω is the angular frequency, ($\omega = 2\pi f$ where f is the frequency (Hz)), E_0 is the peak voltage (V), I_0 is the peak current (A), Z_0 is the peak impedance (Ω) and $\varphi(\omega)$ is the phase shift at any frequency (radians). Further information on the theoretical background of EIS can be found elsewhere [7], [23]–[25].

III. Probe Geometries

In this work, three different probe geometries have been constructed and simulated using ANSYS HFSS to plot the electric field distribution. These designs were then imported into ANSYS Circuit and simulations were run using an ideal sinewave current source and an ideal voltmeter. All three geometries are compatible with TFT and the properties of the dielectric pastes used were taken from real data from the Thick-Film pastes datasheets. The electrodes for all cells were made of gold whilst, the dielectric paste used to control the exposed electrode area was ESL4905-C (Electro Science). To enhance the structural integrity of the cells, PVC-based casing was constructed, further ensuring that the distance between the substrates would be maintained in real life.

A. Planar Thick-Film Probe

The first probe (Planar) that was constructed was the simple, planar configuration with four electrodes. The connections to the current source and voltmeter were made in air whilst only the bottom section (26 mm) of the electrodes was exposed to the MUT. The electronic configuration used and the structural details are shown in Fig. 2. It was expected that this design would experience major fringing effects with respect to frequency, conductivity/resistivity and dielectric constant of the MUT. This drawback would invalidate the very important assumption that the voltage at the voltage electrodes is proportional to the voltage applied at the interface of the MUT and the current electrodes.

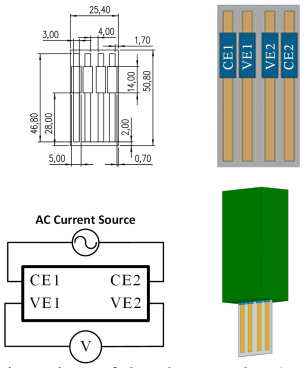

Fig. 2: (top left) Dimensions of the planar probe, (top right) top view of the planar probe, (bottom left) circuit connections to the probe and (bottom right) a 3D image. (Current Electrode (CE), Voltage Electrode (VE)).

B. 3D Thick-Film Probe

The second probe was constructed in a 3D configuration by having two substrates facing each other. The structural details of the 3D Thick-Film probe (3D TF) are shown in Fig. 3.

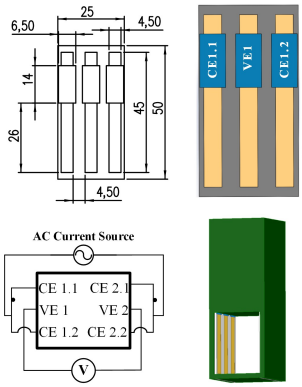

Fig. 3: (top left) Dimensions of the 3D Thick-Film Probe, (top right) top view of the probe, (bottom left) circuit connections to the probe, and (bottom right) a 3D image.

The use of two substrates facing each other was believed to improve the uniformity of the electric field distribution giving a more linear relationships between frequency, MUT properties and the calculated impedances. The current electrodes of this design have two sections, one on each side of the voltage electrode to increase the field uniformity. These two sections were externally connected together and to the current source as shown in the bottom schematic of Fig. 3.

C. 3D Thick-Film Probe with Guards

The third geometry (3D TFwG) is similar to the second one but the electrode dimensions and arrangement was very different. In this design, the two sides of the current electrode are connected on the substrate fully surrounding the voltage electrode. The cross-sectional area of the current electrode was significantly increased and the distance between the current electrode and the voltage electrode was significantly decreased (1 mm) but still maintaining a gap to eliminate any shorting.

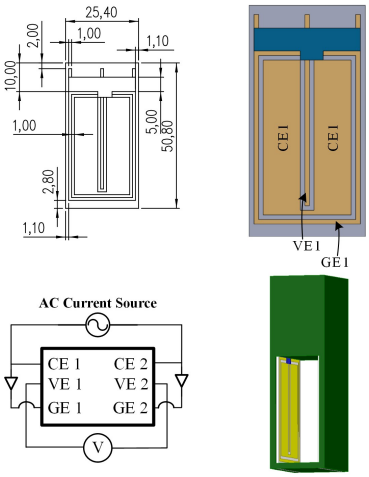

Fig. 4: (top left) Dimensions of the 3D Thick-Film Probe with guards, (top right) top view of the probe, (bottom left) circuit connections to the probe and (bottom right) a 3D image. (Guard Electrode (GE)).

In applications where the MUT can't be contained within a closed probe, controlling the electric field distribution is of significant importance. Therefore, in this design a guard electrode was introduced around the current electrode to control the electric field distribution without enclosing the MUT. This was believed to subsequently increase the accuracy and sensitivity of the probe. For this design, the circuit connections and the electronics are as shown in Fig. 4 with the addition of two buffer amplifiers taking the voltage applied at the current electrodes and using it as input to the guard electrodes with the same phase.

IV. Electric Field Distributions

For the electric field distribution simulations only, a voltage was applied to the current electrodes instead of current, due to the inability of the software to apply current. However, for the rest of the simulations, the circuit and electromagnetic simulators were used in parallel in order to correctly apply current instead of voltage. For the electric field distribution simulations, the applied voltage at the current electrodes was ±10 mV for all probes. In these simulations, the four extremes were considered to emphasize the effect of the MUT's conductivity/resistivity and relative permittivity on the field distributions. The electric field distribution was plotted on a plane of 50x50 mm^2 and was located at the center of the exposed electrode area for all probes.

A. Planar Thick-Film Probe

The electric fields of the planar probe were plotted at 1 kHz and 1 MHz in water-like mediums with conductivities of 0.2 and 4 mS/cm and dielectric constants of 5 and 81 (Fig. 5 and Fig. 6). The values were chosen based on the range of conductivities and dielectric constants that could be found in water-like mediums such as wet soil and aqueous solutions.

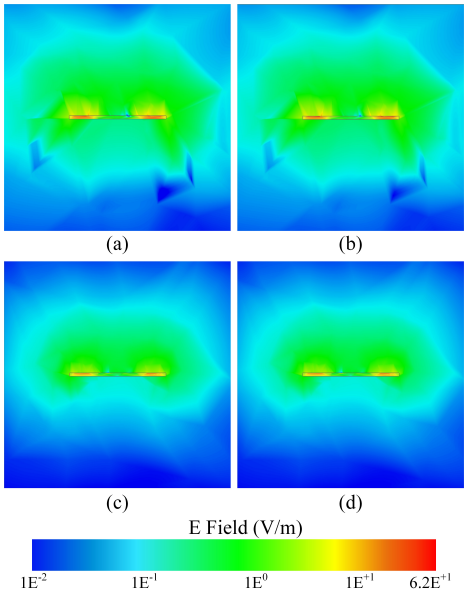

Fig. 5: Electric field distribution in a water-like medium with a dielectric constant of 5. The mediums have conductivities of 0.2 mS/cm (a) at 1 kHz and (b) 1 MHz and 4 mS/cm at (c) 1 kHz and (d) 1 MHz.

The simulation results of the electric field suggest that the electric field distribution highly depends on the conductivity/resistivity of the medium, whilst it is less affected by the dielectric constant and the frequency of the input signal. Due to this fringing of the electric field distribution with changing MUT properties, the measured voltage at the voltage electrodes will not only depend on the strength of the field. It will depend on the changes in the field distribution, which will

in turn give a non-linear relationship with the MUT properties. Additionally, the electric field strength at the voltage electrodes greatly decreases compared to the electric field around the current electrode. This will subsequently decrease the sensitivity of the probe to detect any voltage or phase shift changes at the current electrodes.

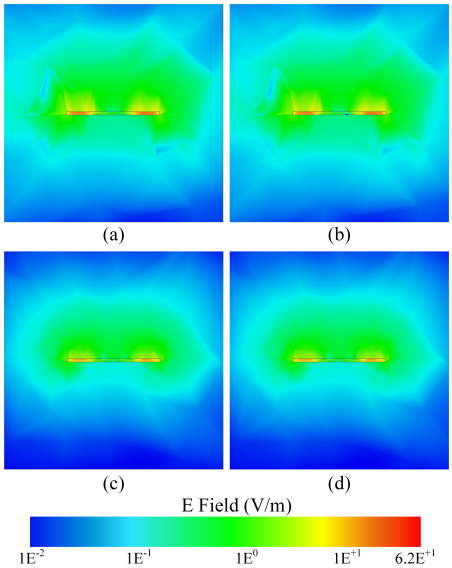

Fig. 6: Electric field distribution in a water-like medium with a dielectric constant of 81. The mediums have conductivities of 0.2 mS/cm at (a) 1 kHz and (b) 1 MHz and 4 mS/cm at (c) 1 kHz and (d) 1 MHz.

B. 3D Thick-Film Probe

Identical medium configurations were tested with the 3D TF probe and the results are shown in Fig. 7 and Fig. 8.

In this case, the electric field distribution is significantly worse than the previous case in terms of field strength around the voltage electrodes. A major field drop can be seen between the two voltage electrodes, which will decrease the sensitivity of the probe even more compared to the planar electrode arrangement.

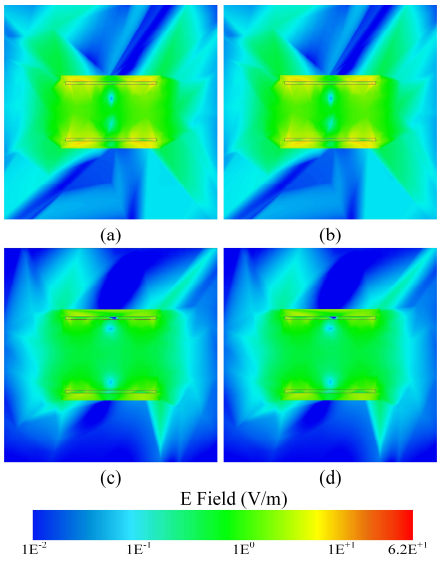

Fig. 7: Electric field distribution in a water-like medium with a dielectric constant of 5. The mediums have conductivities of 0.2 mS/cm at (a) 1 kHz and (b) 1 MHz and 4 mS/cm at (c) 1 kHz and (d) 1 MHz.

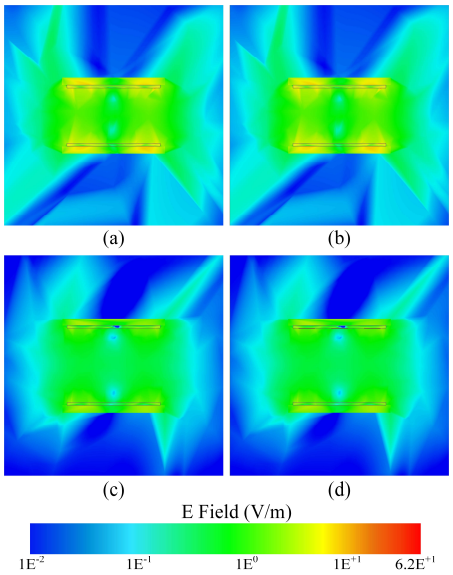

Fig. 8: Electric field distribution in a water-like medium with a dielectric constant of 81. The mediums have conductivities of 0.2 mS/cm at (a) 1 kHz and (b) 1 MHz and 4 mS/cm at (c) 1 kHz and (d) 1 MHz.

On the other hand, the electric field between the two substrates is better distributed but a lot of energy is lost on the outer sides of the current electrodes. Although, the voltage at the voltage electrodes will be closer to the voltage at the current electrodes in this design, the electric field distribution also depends on the frequency of the input signal and the MUT properties. This design has the advantage that the distance between the electrodes can be modified. This is important because the load that the current source will see can be controlled and also that if the medium is not homogeneous, a much better approximation of the MUT properties can be achieved by averaging a larger volume.

C. 3D Thick-Film Probe with Guards

The electric field distributions of the 3D TFwG probes are shown in Fig. 9 & Fig. 10.

Sections (a) and (b) of Fig. 9 & Fig. 10 show the field distribution when the guard electrodes are disabled whilst, sections (c), (d), (e) and (f) show the field distribution with the guards enabled. Comparing the field distribution between those two cases, the field within the probe is significantly improved when the guards are enabled since the electric field strength at the edges of the current electrodes does not change with enabled guards. This ensures that the field strength at the edge is maintained hence minimizing any fringing effects. Additionally, it can be seen that there is a field strength concentration at the voltage electrodes, which is what is required for better sensitivity of the probe. Although from the figures the electric field outside the probe is majorly affected by conductivity/resistivity, frequency and dielectric constant, the changes are coming from the guard electrodes and not the current electrodes. Therefore, this design is by far superior compared to the other two in multiple ways.

In the next section, circuit simulations were performed to compare the performance of the probes.

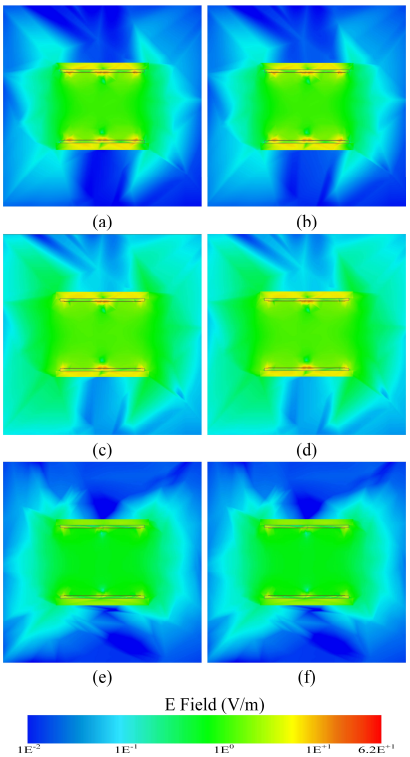

Fig. 9: Electric field distribution in a water-like medium with a dielectric constant of 5. The mediums have conductivities of 0.2 mS/cm at (a) 1 kHz and (b) 1 MHz without enabling the guards, whilst (c) and (d) are the same mediums with guards enabled. The medium in (e) and (f) has conductivity of 4 mS/cm at (e) 1 kHz and (f) 1 MHz with enabled guards.

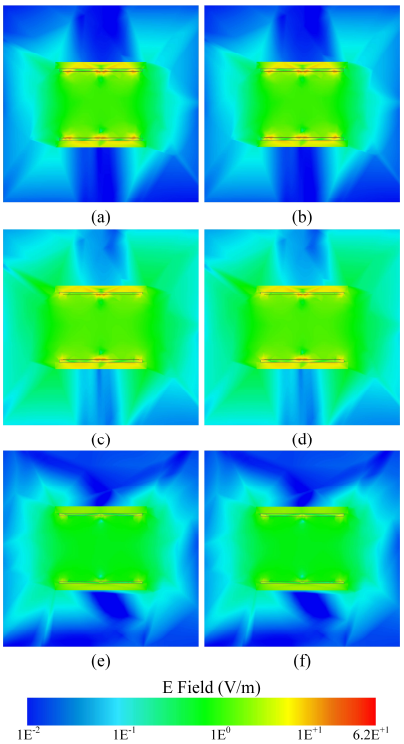

Fig. 10: Electric field distribution in a water-like medium with a dielectric constant of 81. The mediums have conductivities of 0.2 mS/cm at (a) 1 kHz and (b) 1 MHz without enabling the guards, whilst (c) and (d) are the same mediums with guards enabled. The medium in (e) and (f) has conductivity of 4 mS/cm at (e) 1 kHz and (f) 1 MHz with enabled guards.

V. Performance Comparison

The probes were imported directly to ANSYS Circuit and co-simulations were performed to investigate and compare their performance. In these simulations, all cases were simulated using an ideal, differential current source for more accurate results. For each circuit simulation a corresponding electromagnetic simulation was performed. The input current amplitude used was 10 μA to ensure that the applied voltages were not higher than 25-30 mV. Usually, EIS requires low voltages so that no chemical reactions are generated on the electrodes. Transient simulations were performed with 1 million steps per cycle and the readings were taken after 1 thousand cycles of the input signal to allow enough settling time of the electric field.

A. Relationship between Current & Voltage Electrodes

The first and most important characteristic of the probe to check was whether the voltage electrodes could track the voltage of the current electrodes. Fig. 11 shows how the voltage of the voltage electrode changes with the voltage of the current electrodes in mediums with conductivities 0.2, 0.5, 1, 2 and 4 mS/cm and a dielectric constant of 20 at 1 kHz. A middle value of 20 for relative permittivity was chosen as an indicative value. The frequency of 1 kHz was chosen so that there would be insignificant phase shift, hence no significant phase difference between the voltage and current electrodes, to affect the voltage amplitude.

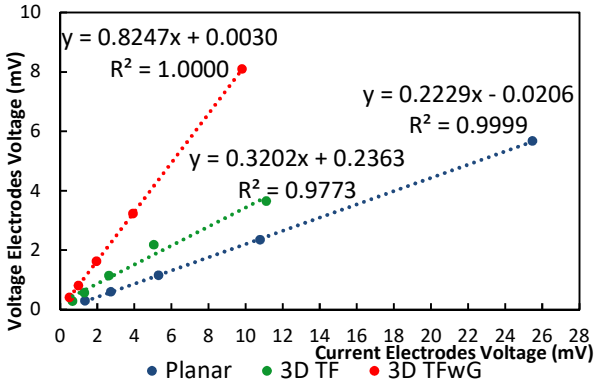

Fig. 11: Voltage measured at the current electrodes versus the voltage at the voltage electrodes.

The voltage electrodes from all designs follow the voltage of the current electrodes but probe 3D TF shows the least linear relationship with an R^2 value of 0.9773. The planar design on the other hand, shows a very linear relationship with an R^2 of 0.9999 whilst the 3D TFwG show an even better linearity with R^2 of 1. Other than the linearity, the sensitivity/slope of the graph is the lowest for the planar design and highest for the 3D TFwG probe. This indicates that the voltage measured at the voltage electrodes will be significantly closer to the voltage of the current electrodes for the 3D TFwG probe compared to the other two, resulting in a more sensitive probe.

Other than the relationship between the voltages of the current and voltage electrodes, the phase shift between the current and voltage is another important factor. It determines the imaginary part of the impedance, which in turn affects the equivalent circuit model. Fig. 12 shows the phase shift at the current electrodes versus the phase shift observed at the

voltage electrodes in conductivities of 0.2, 0.5, 1, 2 and 4 mS/cm in a medium with dielectric constant of 20 at 1 MHz.

In this case, the planar configuration shows the most linear response with the 3D TF probe showing the worst linearity. R^2 values for all three probes were higher than 0.9942 showing the linearity of the relationship but the 3D TFwG probe showed a slope closer to 1, which means that there will be a much less delay between the signal on the current electrodes and the signal received by the voltage electrodes.

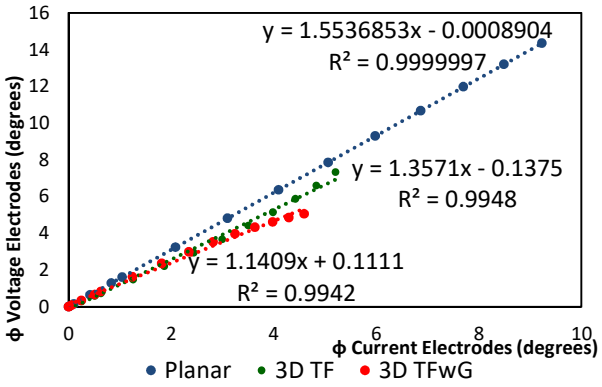

Fig. 12: Phase shift at the current electrodes versus phase shift at the voltage electrodes.

Based on these results, the 3D TFwG probe shows significantly higher performance in terms of tracking the voltage of the current electrodes. In terms of tracking the phase shift, all three perform adequately, however in all three probes there is a delay in the signal between the current electrodes and the voltage electrodes that can be misinterpreted as phase shift. Hence, the 3D TFwG probe with a slope of 1.14 shows less delay allowing for more accurate measurements.

B. Probes' Outputs versus Frequency

The ability of the probe to sense changes in the phase between the input current and the voltage measured at the voltage electrodes is another important characteristic of the probe. Fig. 13 and Fig. 14 show the relationship between the measured voltage at the voltage electrodes and the phase shift φ with frequency. The plotted results are in a medium with conductivity of 0.2 mS/cm (resistivity of 50 Ωm) and a dielectric constant of 20 for the same reasons explained above.

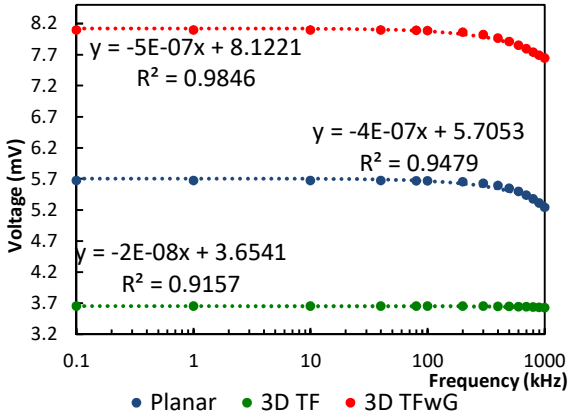

Fig. 13: Voltage measured at the voltage electrodes versus frequency.

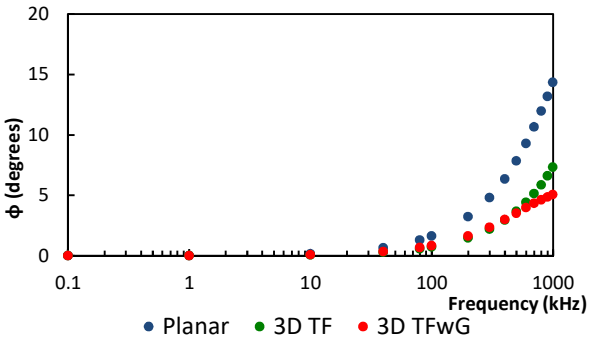

Fig. 14: Phase shift φ at the voltage electrodes versus frequency.

From the graphs, the 3D TFwG probe shows superior performance in terms of slope and linearity for the voltage amplitude. In terms of the phase shift, although it seems like it experiences the lowest phase shift, it is the only one of the three that appears closer to the plateau at 1MHz, which can be attributed to the lower total impedance measured.

C. Probes' Outputs & MUT Parameters

The most important characteristic of the probes is its ability to detect the MUT's properties and the linearity of that relationship. The two most important properties of the MUT is the conductivity/resistivity and the dielectric constant or relative permittivity. In order to investigate those relationships, the measured voltage at the voltage electrodes at 1 kHz was plotted against resistivity for all three probes.

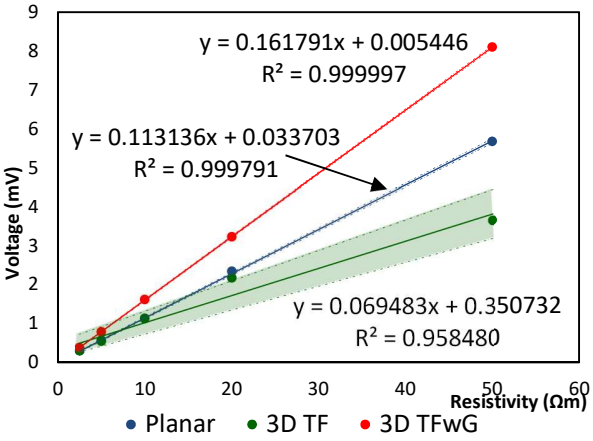

Fig. 15: Voltage at the voltage electrodes at 1 kHz versus the conductivity of the MUT. The shaded area represents the standard error for each probe.

From Fig. 15, the 3D TFwG probe shows significantly superior linearity and smaller standard error compared to the other two probes. The measured voltage is directly proportional to resistivity ($conductivity = 1/resistivity$), where conductivity is measured in Siemens per meter ($S \cdot m^{-1}$) and resistivity in Ohm meters ($\Omega \cdot m$). The 3D TFwG probe has a sensitivity of 0.162 mV/Ωm and a standard error of 0.002, whilst the planar probes has a sensitivity of 0.113 mV/Ωm and standard error of 0.003 and the 3D TF probe has sensitivity of 0.069 mV/Ωm with 0.032 standard error.

Fig. 16 shows the phase shift versus the dielectric constant of the medium with conductivity of 0.2 mS/cm (resistivity of 50 Ωm) at 1 MHz. All three probes show a linear relationship between the phase shift and the dielectric constant.

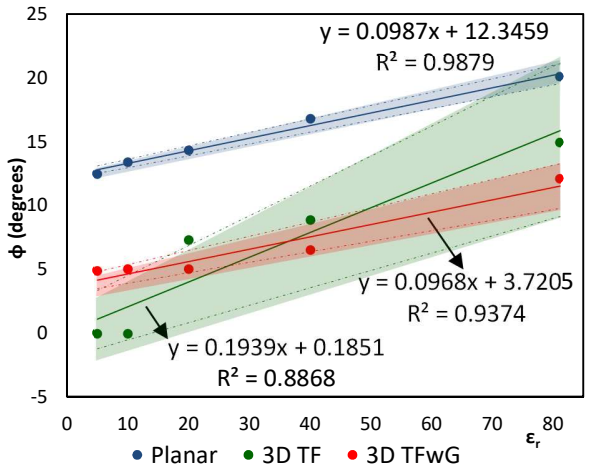

Fig. 16: Phase shift at 1 MHz at the voltage electrodes versus the dielectric constant. The shaded area represents the standard error for each probe.

The planar and 3D TFwG probes show a sensitivity of approximately 0.1 °/ε_r, whilst the 3D TF probe shows a sensitivity of 0.2 °/ε_r. However, although the 3D TF probe shows a higher sensitivity, the standard error is 3.32, which is not adequate for any application. The 3D TFwG probe has a standard error of 0.88 and the planar probe of 0.39. It is clear that the planar probe shows better performance in the relative permittivity range of 5-81. Yet, when the normalized phase shift is plotted versus the relative permittivity (Fig. 17), the 3D TFwG probe shows more than 3.6 times higher sensitivity (0.024 °/ε_r) than the planar probe (0.0074 °/ε_r) in the range of 20-81. On the other hand, in the range of 5-20, the planar probe shows 4.8 times higher sensitivity (0.0096 °/ε_r) than the 3D TFwG probe (0.002 °/ε_r).

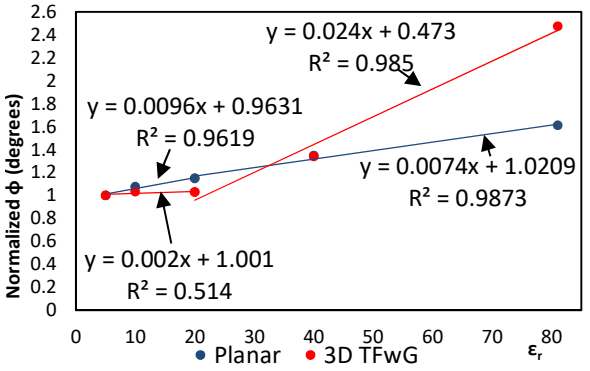

Fig. 17: Normalized phase shift at 1 MHz at the voltage electrodes versus the dielectric constant.

D. Comparison Summary

In order to properly compare the performance of the three probes, all the important parameters have been included in Table I including sensitivities, linearities and standard errors.

It is concluded that for conductivity/resistivity measurements, the 3D TFwG probe shows significant superiority to the other probes in terms of sensitivity, linearity and standard error. Additionally, it can more accurately track the voltage of the current electrodes and shows the least delay between the signal on the voltage electrodes and the current electrodes.

TABLE I
COMPARISON SUMMARY

Parameter	*Planar*	*3D TF*	*3D TFwG*
Sensitivity			
Resistivity (mV/Ωm)	0.113	0.069	0.162
Relative Permittivity (°/ε_r)	0.1	0.2	0.1
Voltage of Current vs Voltage Electrodes (mV/mV)	0.22	0.32	0.82
Phase shift Current vs Voltage Electrodes (°/°)	1.55	1.36	1.14
Linearity (R^2)			
Resistivity	0.9998	0.958	0.999997
Relative Permittivity	0.9879	0.8868	0.9374
Voltage of Current vs Voltage Electrodes	0.9999	0.9773	0.999998
Phase shift Current vs Voltage Electrodes	1	0.9948	0.9942
Voltage with Frequency	0.95	0.92	0.98
Standard Error (S_{yx})			
Resistivity	0.003	0.032	0.002
Relative Permittivity	0.39	3.32	0.88

In terms of relative permittivity, the planar and 3D TFwG probes show similar sensitivities for the range of 5-81, however the planar probe shows more than half of the standard error experienced by the 3D TFwG probe. Yet, by investigating the normalized phase shift experienced by the 3D TFwG probe, it shows more than 3.6 times higher sensitivity than the planar probe. On the other hand, in the range of 5-20, the planar probe shows 4.8 times higher sensitivity than the 3D TFwG probe. Therefore, for MUT's with dielectric constant of 5-20, the planar probe performs better but for MUT's with dielectric constant of 20-81, the 3D TFwG probe performs better. It has to be noted here that the better performance of the planar probe at the lower end of the scale can be attributed to the higher delay of the signal between the voltage and current electrodes, which unless manually eliminated, will generate inaccurate results.

VI. Equivalent Circuit Model

It is common practice to construct equivalent circuit models obtained by EIS measurements because each of the components can represent a physical parameter of the system/MUT. The most common equivalent circuit at the current electrodes is the Simplified Randles Cell [7] (Fig. 18).

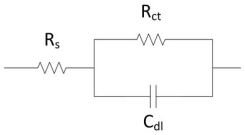

Fig. 18: Simplified Randles Cell.

where R_s is the solution's resistance (Ω), R_{ct} is the charge transfer or polarization resistance (Ω) and C_{dl} is the double layer capacitance (C). The impedance of the Simplified Randles Cell at any frequency is defined as:

$$Z(\omega) = R_s + \frac{R_{ct}}{R_{ct}^2\omega^2C_{dl}^2+1} - j\frac{R_{ct}^2\omega C_{dl}}{R_{ct}^2\omega^2C_{dl}^2+1} \quad (2)$$

Once the impedance of the MUT is found by (1), the values of

the lumped components based on the Simplified Randles Cell can be calculated from (2) based on the condition that at low frequencies:

$$Z(\sim 0) \approx R_s + R_{ct} \tag{3}$$

Hence:

$$R_s = Z(\sim 0) - R_{ct} \tag{4}$$

$$R_{ct} = \frac{Z_j(\omega)^2}{Z(\sim 0) - Z_r(\omega)} - Z_r(\omega) + Z(\sim 0) \tag{5}$$

$$C_{dl} = \left(\frac{Z(\sim 0) - Z_r(\omega)}{(Z_r(\omega) - Z(\sim 0) + R_{ct}) R_{ct}^2 \omega^2} \right)^{\frac{1}{2}} \tag{6}$$

Where $Z(\sim 0)$ is the impedance at very low frequencies within the kinetically controlled region (Ω), $Z_r(\omega)$ is the real part of the impedance at any frequency and $Z_j(\omega)$ is the imaginary part of the impedance at any frequency.

R_s and R_{ct} represent some properties of the MUT and obtaining them is usually the objective when performing EIS. R_s is the apparent resistance of the MUT and there are numerous techniques to obtain the real resistance depending on the MUT. R_{ct} on the other hand, is the charge transfer resistance, which for aqueous solutions is defined as [7]:

$$R_{ct} = \frac{RT}{F^2 k^0 C} \tag{7}$$

Where R is the molar gas constant ($m^2 kg\ s^{-2} K^{-1} mol^{-1}$), T is the temperature (K), F is the Faraday constant ($C\ mol^{-1}$), k^0 is the heterogeneous electron transfer rate constant and C is the concentration of the electroactive species (M) if the MUT is a solution.

C_{dl} is the double layer capacitance, which based on the Gouy-Chapman-Stern model, in aqueous solutions is defined as [26]:

$$\frac{1}{C_{dl}} = \frac{x}{\varepsilon \varepsilon_0} + \frac{1}{\left(\frac{2\varepsilon \varepsilon_0 z^2 e^2 n^0}{kT} \right)^{1/2} \cosh\left(\frac{zeV_2}{2kT} \right)} \tag{8}$$

where x is the distance between the electrode and the plane of closest approach of the centers of the counterions (m), e and z are the electron charge and the valency of the ion, n^0 is the bulk concentration of ions (M), k is Boltzmann's constant ($J \cdot K^{-1}$), T is the absolute temperature (K) and V_2 is the potential at the distance x with respect to bulk solution (V).

For the example of 0.2 mS/cm and relative permittivity of 20, the equivalent circuit was constructed with the component values shown in Table II. The impedances used to extract the values were the voltages and phase shifts experienced by the current electrodes. In reality, the conversion between the voltage and phase shift between what is recorded at the voltage electrodes and what is experienced at the current electrodes, must be performed before obtaining these values.

Based on the extracted parameters for the equivalent circuit, the behaviour of all three probes were plotted on a Nyquist plot shown in Fig. 19.

TABLE II
COMPONENT VALUES

Probe	R_s (Ω)	R_{ct} (Ω)	C_{dl} (pF)
Planar	1448.75	1099.19	59.82
3D TF	833.25	279.20	232.71
3D TFwG	775.14	206.07	340.72

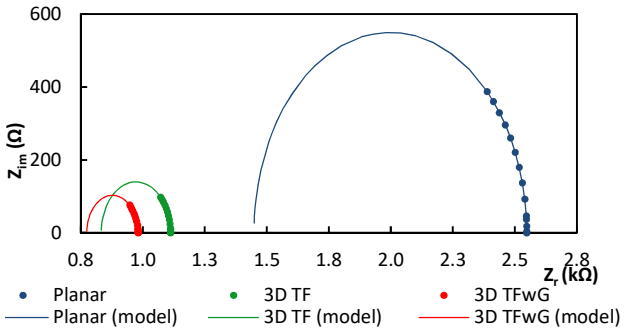

Fig. 19: Nyquist plots for the three probes in a medium of 0.2 mS/cm conductivity and a dielectric constant of 20.

The equivalent circuit model agrees with the expected behavior of the medium. From the Nyquist plot, the lower resistance experienced by the probes between the current electrodes is more obvious for the 3D TF and 3D TFwG probes giving a more balanced ratio between the imaginary and real values of the MUT's impedance.

VII. Experimental Validation

The use of the Simplified Randles' model was evaluated experimentally in aqueous solutions of known conductivity/resistivity and dielectric constant. It is important to note that the adopted model (Simplified Randles' model) does not take into account the Warburg impedance i.e. the mass transport, hence it is known to be inaccurate at lower concentrations and frequencies. However, at higher frequencies (>~200 kHz) the model is significantly accurate and that is why it is widely used for simplicity, since Warburg impedance is a very difficult component to model. The simulation software does not take into account the mass transport parameter, hence the simulated results agree with the Simplified Randles' model.

A. Probe Fabrication

The 3D TFwG probe was printed on 96% alumina substrate. The high purity ink used for the gold electrodes was ESL-8844 (Electro Science) whilst the dielectric paste used was ESL 4905-C (Electro Science). The probes also included soldering pads (5 mm x 5 mm) using an ESL 9512-G ink (Electro Science) at the end of the gold electrodes for external connections. The probes were connected to an external circuit through short (<100mm) wires, to minimize the effect of wire capacitances. Furthermore, a 3D printed (PLA) holder was used to hold the 2 substrates at a distance of 15 mm, whilst the connections were waterproofed using hot glue.

B. Experimental Setup

In order to test the probe, a potassium chloride solution was chosen because it is widely used as a conductivity/resistivity standard for instrument calibration. A 0.2 mS/cm (50 Ωm) KCl solution was prepared by dissolving KCl (BDH 101984L AnalaR) in deionized water and the conductivity of the solution was confirmed using a calibrated, commercially-available conductivity meter (HANNA Instruments HI 993310). At low concentrations, the dielectric constant of

aqueous solutions can be assumed to be ~80 [27]. All experiments were performed at room temperature (25°C±2°C).

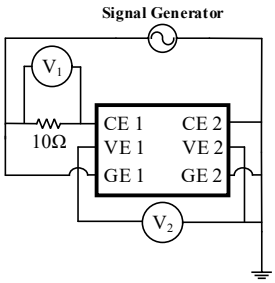

Fig. 20: Schematic of the instrumentation used.

All electrodes on one side of the probe were connected to the ground (single-ended and not differential as in the simulations). The current electrode on the other substrate (CE1) was connected in series with a 9.783 Ω resistor, measured using an RLC meter (Agilent E4980A), whilst the guard electrode (GE) was connected directly to the signal generator (Agilent 33220A). The voltages across the resistor and across the voltage electrodes were measured using an oscilloscope (LeCroy Wavepro 7300A). The input voltage from the signal generator was manually adjusted to ensure that the current through the resistor, and hence the system, was maintained at 2 mA. The phase shift between the voltage across the resistor and the voltage across the probe was calculated by a standard function of the oscilloscope. A schematic of the instrumentation used is shown in Fig. 20.

C. *Results*

The voltage measured across the voltage electrodes was used to calculate the voltage across the current electrodes using the equation obtained from the simulations and the real and imaginary parts of the impedances were plotted on a Nyquist plot shown in Fig. 21.

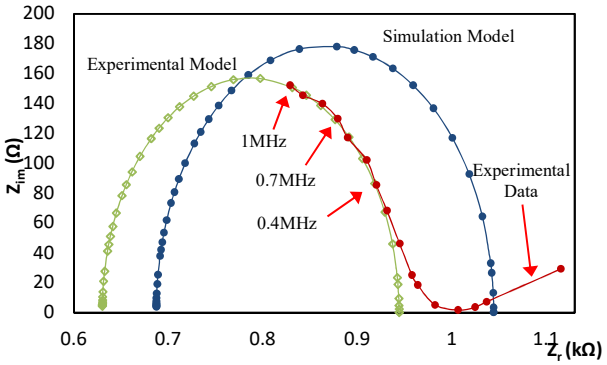

Fig. 21: Nyquist plots obtained for the 3D TFwG in a KCl solution of 0.2 mS/cm conductivity and a dielectric constant of~80.

The simulated and fitted component values based on the Simplified Randles' Model are provided on Table III.

The experimental results suggest that the Simplified Randles' model can be used at frequencies >200 kHz in a medium with conductivity of 0.2 mS/cm (50 Ωm) and a dielectric constant of ~80. Mediums with lower conductivities and higher dielectric constants will be more affected by the Warburg impedance, whilst higher conductivities and lower dielectric constants will be less affected as the ionic mass transport will be much higher.

TABLE III
MODEL COMPONENT VALUES

	R_s (Ω)	R_{ct} (Ω)	C_{dl} (pF)
Simulations	687.1	357.1	416
Experimental	630	314	380
	658.55±4%	335.55±6%	398±4%

There is a difference between the simulated component values and the experimentally obtained values, which can be explained by experimental and measurement errors. Most prominent sources of errors are minor concentration differences, minor differences in the distance between the two substrates (±0.5 mm), whilst the most significant source of errors is the measurement method. The current is controlled by the potential difference across the resistor (~39 mV_{p-p}), which is prone to errors (±2 mV) due to the low measurement accuracy at low amplitude levels. Furthermore, low phase shift calculations are more prone to errors rather than higher phase shifts, especially when measured with ±2 mV noise levels and probe capacitances (11pF each) comparative to that of the cell.

The experimental values, R_s and R_{ct} are lower than the simulated due to parasitic resistances that provide an alternative path for current to ground, decreasing the actual current flowing in the cell. The measured capacitance on the other hand was expected to be higher than the simulated due to parasitic capacitances, yet it was found to be slightly lower. However, the values are within ±6% of each other and as such can easily be attributed to experimental measurement error as opposed to any systematic error. Therefore, the Simplified Randles' model can be used for higher frequencies, as the simulations have predicted and the measured impedances at ~1 kHz is representative of the conductivity/resistivity of the solution. Translating the measured voltage at 1 kHz to conductivity based on the simulation-obtained equation, the medium has a conductivity of approximately 0.19 mS/cm, which is very close to the measured conductivity using the commercially-available conductivity meter.

VIII. CONCLUSIONS

In this paper, three different, screen-printed EIS probes that do not require the MUT to be fully enclosed and could be used in harsh environments, have been constructed and simulated in mediums of various conductivities/resistivities and dielectric constants. The drawbacks and advantages of each probe have been reported along with techniques on how they can be overcome by modified geometries.

The simulated results were used to construct equivalent circuits using the Simplified Randles' model, whilst the electrical parameters of the models' components have been extracted and presented. The proposed model has been verified and agrees with experimental results at higher frequencies where the Warburg impedance is negligible.

These probes can be used as real-time sensors and can be deployed directly in the MUT such as soil or concrete to monitor the MUT's resistivity or dielectric constant. Relationships between these parameters and other MUT properties such as salinity and water content or moisture have

been reported in the literature and having IoT-compatible sensors for them is a major requirement for many automated condition monitoring systems. Future work involves the fabrication and testing of the probe in various mediums and comparing the simulated and experimentally derived results.

ACKNOWLEDGMENTS

The authors would like to thank the University of Cyprus for the internal funds and would like to gratefully acknowledge the support of NVIDIA Corporation with the donation of the Quadro P5000 GPU used for this research.

REFERENCES

[1] H. Jiang, A. Sun, A. G. Venkatesh, and D. A. Hall, "An audio jack-based electrochemical impedance spectroscopy sensor for point-of-care diagnostics," *IEEE Sens. J.*, vol. 17, no. 3, pp. 589–597, 2017.

[2] M. Lee, J. Hwang, and H. Yoe, "Agricultural production system based on IoT," *Proc. - 16th IEEE Int. Conf. Comput. Sci. Eng. CSE 2013*, pp. 833–837, 2013.

[3] M. Sophocleous and J. Georgiou, "Precision agriculture: Challenges in sensors and electronics for real-time soil and plant monitoring," *2017 IEEE Biomed. Circuits Syst. Conf.*, pp. 1–4, 2017.

[4] B. E. Conway, J. O. Bockris, and R. E. White, Eds., *Modern Aspects of Electrochemicstry*. KLUWER ACADEMIC PUBLISHERS, 2002.

[5] A. Carullo, F. Ferraris, M. Parvis, A. Vallan, E. Angelini, and P. Spinelli, "Low-cost electrochemical impedance spectroscopy system for corrosion monitoring of metallic antiquities and works of art," *IEEE Trans. Instrum. Meas.*, vol. 49, no. 2, pp. 371–375, 2000.

[6] M. Grossi, G. Di Lecce, T. G. Toschi, and B. Riccò, "Fast and accurate determination of olive oil acidity by electrochemical impedance spectroscopy," *IEEE Sens. J.*, vol. 14, no. 9, pp. 2947–2954, 2014.

[7] E. P. Randviir and C. E. Banks, "Electrochemical impedance spectroscopy: An overview of bioanalytical applications," *Anal. Methods*, vol. 5, no. 5, pp. 1098–1115, 2013.

[8] J. K. Atkinson and M. Sophocleous, "A novel thick-film screen printed electrical conductivity sensor for measurement of liquid and soil conductivity," *IEEE SENSORS 2014 Proc.*, vol. 2014-Decem, no. December, pp. 86–89, 2014.

[9] M. Sophocleous, P. Savva, M. F. Petrou, J. K. Atkinson, and J. Georgiou, "A durable, screen-printed sensor for in-situ and real-time monitoring of concrete?s electrical resistivity suitable for smart buildings/cities and IoT," *IEEE Sensors Lett.*, 2018.

[10] M. Sophocleous and J. K. Atkinson, "A novel thick-film electrical conductivity sensor suitable for liquid and soil conductivity measurements," *Sensors Actuators, B Chem.*, vol. 213, pp. 417–422, 2015.

[11] J. K. Atkinson, M. Glanc, M. Prakorbjanya, M. Sophocleous, R. Sion, and E. Garcia Breijo, "Thick film screen printed environmental and chemical sensor array reference electrodes suitable for subterranean and subaqueous deployments," *Microelectron. Int.*, vol. 30, no. 2, pp. 92–98, 2013.

[12] M. N. Nabighian, *Electromagnetic Methods in Applied Geophysics, Theory, vol.1*. 2006.

[13] M. Sophocleous, "Electrical Resistivity Sensing Methods and Implications," in *Electrical Resistivity and Conductivity*, 2017.

[14] M. Sophocleous, *Thick-Film Underground Sensors*. LAP LAMPERT Academic Publishing, 2016.

[15] A. Ruiz-Vargas, A. Ivorra, and J. W. Arkwright, "Design, Construction and Validation of an Electrical Impedance Probe with Contact Force and Temperature Sensors Suitable for in-vivo Measurements," *Sci. Rep.*, vol. 8, no. 1, pp. 1–11, 2018.

[16] J. A. Gutiérrez Gnecchi, A. G. T. Chávez, G. M. Chávez Campos, V. H. O. Peregrino, and E. Marroquin Pineda, "Soil water infiltration measurements using electrical impedance tomography," *Chem. Eng. J.*, vol. 191, pp. 13–21, 2012.

[17] M. Weigand and A. Kemna, "Imaging and functional characterization of crop root systems using spectroscopic electrical impedance measurements," *Plant Soil*, vol. 435, no. 1–2, pp. 201–224, 2019.

[18] G. D'Antona and L. Rocca, "Electrical impedance tomography for underground pollutant detection and polluted lands reclaiming monitoring," *Conf. Rec. - IEEE Instrum. Meas. Technol. Conf.*, vol. 2, no. May, pp. 1035–1038, 2002.

[19] L. Bar-On, A. Jog, and Y. Shacham-Diamand, "Four point probe electrical spectroscopy based system for plant monitoring," *Proc. - IEEE Int. Symp. Circuits Syst.*, vol. 2019-May, pp. 6–10, 2019.

[20] R. Analytical, "Conductivity Theory and Practice Guide," 2004.

[21] D.-T. Devices Ltd, "ML3ThetaProbe." pp. 1–47, 2017.

[22] GAMRY, "Basics of Electrochemical Impedance Spectroscopy," *Appl. Note AC*, no. 1, pp. 1–17, 2010.

[23] C. Byoung-Yong and P. Su-Moon, "Electrochemical Impedance Spectroscopy," *Annu. Rev. Anal. Chem.*, vol. 3, pp. 207–229, 2010.

[24] M. Grossi and B. Riccò, "Electrical impedance spectroscopy (EIS) for biological analysis and food characterization: A review," *J. Sensors Sens. Syst.*, vol. 6, no. 2, pp. 303–325, 2017.

[25] E. Barsoukov and R. J. . Macdonald, *Impedance Spectroscopy: Theory, Experiment, and Applications*, 2nd ed. Wiley, 2005.

[26] V. Lockett, M. Horne, R. Sedev, T. Rodopoulos, and J. Ralston, "Differential capacitance of the double layer at the electrode/ionic liquids interface," *Phys. Chem. Chem. Phys.*, vol. 12, no. 39, pp. 12499–12512, 2010.

[27] N. Gavish and K. Promislow, "Dependence of the dielectric constant of electrolyte solutions on ionic concentration," *Arxiv*, no. 2, pp. 1–5, 2012.

Marios Sophocleous (M'17) is a Special Scientist at the University of Cyprus since 2016. He obtained his Masters of Engineering degree from the University of Southampton in Mechatronics and his PhD in Thick-Film Underground Sensors in 2016 from the same University. He is an active member of the IEEE community, whilst he has been invited multiple times as a technical and/or organizing committee member for major conferences.

John Atkinson is a Professor of Engineering Science in the Faculty of Engineering and Physical Sciences at the University of Southampton UK where his research interests include thick film technology, electronic instrumentation and sensors. In particular he has been working in the field of thick film (screen printed) sensor arrays for many years. He is editor of the scientific journal Microelectronics International.

Eduardo García-Breijo received the M.S. degree in electronic engineering from the Universitat de València (UV), Spain, in 1997 and the Ph.D. degree from the Universidad Politécnica de Valencia (UPV), in 2004. He is an Assistant Professor of electronic technologies with UPV. He is a member of the Instituto de Reconocimiento Molecular y Desarrollo Tecnológico, UPV. His main areas of interest are the development of printed sensors.

Julius Georgiou (M'98–SM'08) received the M.Eng degree in electrical and electronic engineering and the Ph.D. degree from Imperial College London, London, U.K., in 1998 and 2003, respectively. He is now an Associate Professor at the University of Cyprus. His research interests include Low-power analog and digital ASICs, implantable biomedical devices, bioinspired electronic systems, brain-computer-interfaces (BCIs) and semiconductor device design. Dr. Georgiou is a member of the IEEE Circuits and Systems Society, the BioCAS Technical Committee, and the IEEE Circuits and Systems Society Analog Signal Processing Technical Committee.